Case Studies in Chemical and Environmental Engineering 10 (2024) 100925

Contents lists available at ScienceDirect

Case Studies in Chemical and Environmental Engineering

journal homepage: www.sciencedirect.com/journal/case-studies-in-chemical-and-environmental-engineering

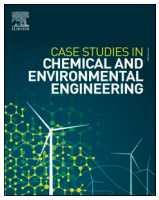

Case Report

Tailoring acid-base properties on metal-free zeolite from Indonesia kaolin to enhance the CO_2 hydrogenation to CH_4

Novia Amalia Sholeha [a,**], Bintang Dewanto [a], Stella Jovita [b], Reva Edra Nugraha [c], Yun Hin Taufiq-Yap [d], Maria Ulfa [e], Anees Ameera Fauzi [f], Aishah Abdul Jalil [g,h], Hasliza Bahruji [i], Didik Prasetyoko [b,*]

[a] College of Vocational Studies, Bogor Agricultural University (IPB University), Jalan Kumbang No. 14, Bogor, 16151, Indonesia
[b] Department of Chemistry, Faculty of Science, Institut Teknologi Sepuluh Nopember, Keputih, Sukolilo, Surabaya, 60111, Indonesia
[c] Department of Chemical Engineering, Faculty of Engineering, Universitas Pembangunan Nasional "Veteran" Jawa Timur, Surabaya, 60294, Indonesia
[d] Department of Chemistry, Faculty of Science, Universiti Putra Malaysia, Serdang, Selangor, Malaysia
[e] Chemistry Education Study Program, Faculty of Teacher Training and Education, Sebelas Maret University, Jl. Ir. Sutami 36A, Surakarta, 57126, Indonesia
[f] Research Center for Biomass and Bioproduct, National Research and Innovation Agency (BRIN), Indonesia
[g] Department of Chemical Engineering, Faculty of Chemical and Energy Engineering, Universiti Teknologi Malaysia, 81310, UTM, Skudai, Johor Bahru, Johor, Malaysia
[h] Centre of Hydrogen Energy, Institute of Future Energy, Universiti Teknologi Malaysia, Skudai, 81310, UTM, Johor Bahru, Johor, Malaysia
[i] Centre of Advanced Material and Energy Science, Universiti Brunei Darussalam, Jalan Tungku Link, BE 1410, Brunei Darussalam

ARTICLE INFO

Keywords:
Metal free catalyst
Basicity
Greenhouse carbon dioxide
Methane
Zeolite

ABSTRACT

The catalytic thermal conversion of carbon dioxide is essential for carbon capture, storage, and utilization, helping to reduce CO_2 emissions and potentially stimulating future economic activities. Zeolite Y, ZSM-5, BEA, and A were synthesized using the hydrothermal technique from Indonesian kaolin to examine the potential use of zeolite as a catalyst without metal nanoparticles. In the absence of metal, catalytic activity for CO_2 methanation relies solely on textural properties and basicity-acidity. Zeolite Y exhibits the highest CO_2 conversion at 36.64 % and attained 100 % of CH_4 selectivity at 400 °C. The exceptional CO_2 conversion of zeolite Y relies on a high basicity level of 1.02 mmol/g, as shown by CO_2-TPD analysis, and a relatively low acid site concentration of 1.48 mmol/g, as determined by NH_3-TPD analysis. ZSM-5, BEA, and zeolite A, demonstrated CO_2 conversion of 29.85 %, 23.86 %, and 12.15 %, respectively. Stability studies revealed ZSM-5 maintains methane (CH_4) selectivity of 94 %, which is only slightly lowered by 6 % for 30 hours, while zeolite Y achieved 90 % selectivity for 26 hours. The presence of mesopores in zeolite ZSM-5 reduced coke or carbon production, maintaining crystalline framework.

1. Introduction

Global warming has been substantially contributed by excessive CO_2 emissions from various human activities and the extensive use of fossil fuels [1]. Strategies for capturing, storing, and utilizing CO_2 are deemed essential for resolving uncontrolled CO_2 emissions [2]. CO_2 hydrogenation by green hydrogen is a promising approach that entails CO_2 conversion into fuels and chemicals, including methane, methanol, ethanol, olefins, and syngas. The Sabatier reaction, known as CO_2 methanation, is thermodynamically advantageous at low pressure [3]. Although methane (CH_4) is less valuable than methanol, ethanol, and light olefins, its production is a straightforward process for carbon conversion. CO_2 methanation is essential in Power-to-Gas technology, as it generates green methane from CO_2 and hydrogen. Ideally, hydrogen must be generated from renewable energy such as wind and solar, and the green methane should be utilized circularly instead of a linear process. In addition to its potential use as a fuel, CH_4 can produce other valuable compounds such as methanol and formaldehyde, through methane partial oxidation [4].

CO_2 methanation is restricted by thermodynamic limitations at temperatures above 400 °C due to its exothermic and reversible nature and competing side reactions [5–7]. A highly active catalyst is required

* Corresponding author.
** Corresponding author.
E-mail addresses: noviaamaliasholeha@apps.ipb.ac.id (N.A. Sholeha), didikp@chem.its.ac.id (D. Prasetyoko).

https://doi.org/10.1016/j.cscee.2024.100925
Received 24 July 2024; Received in revised form 27 August 2024; Accepted 30 August 2024
Available online 31 August 2024

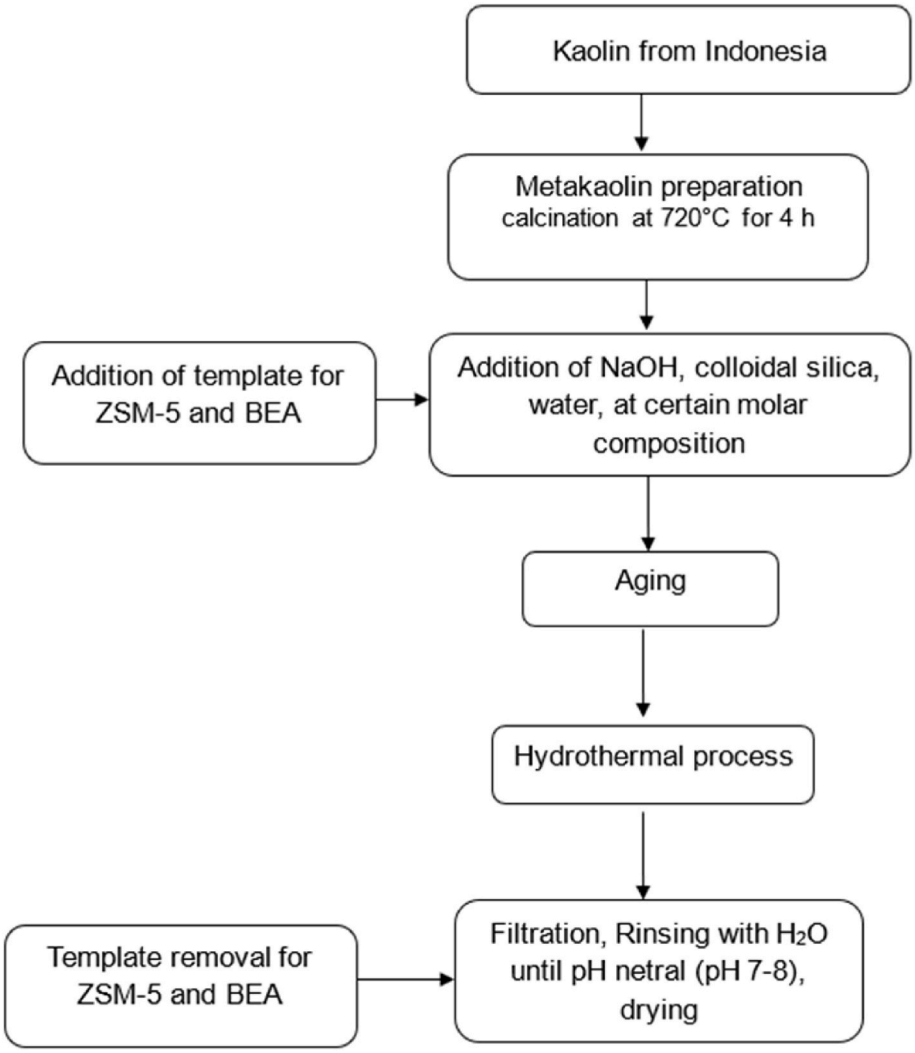

Fig. 1. Flowchart of zeolite synthesis from Indonesian Kaolin.

Table 1
Zeolite's molar ratio preparation.

Sample of zeolite	The ratio of molar zeolite					Aging (h)	Hydrothermal		T_{drying}
	SiO_2	Na_2O	Al_2O_3	H_2O	Template		T (°C)	t (h)	(°C)
Y	10	4	1	180	–	24	100	24	105
ZSM-5	100	10	2	1800	20 TPA	12	80	12	110
					3.85 CTABr		150	24	
A	1.92	3.165	1	128	–	–	100	20	105
BEA	27	1.96	1	240	5 TEA_2O	–	150	48	110

to reduce the kinetic energy barrier during the reduction of the oxidized carbon to CH_4 [8]. A plethora of catalysts have been developed for CO_2 methanation using Ru, Fe, Ni, Co, Rh, Pd, and Pt metal nanoparticles on various support materials [9,10]. A critical issue when using metal for industrial applications is rapid deactivation because of particle sintering and carbon deposition [11]. The commercial viability of CO_2 methanation is dampened by the scarcity and high cost of noble metals [12]. In addition, metal nanoparticles frequently experience a variety of other drawbacks, such as low selectivity, poor durability, toxicity, fuel crossover effects, and adverse environmental impacts. Therefore, it is highly desirable to design catalysts that are readily accessible and cost-effective but demonstrate catalytic performance comparable to noble-metal-based catalysts [13].

Metal-free catalysts have recently gained attention for CO_2 reduction reactions. Examples of such systems include zeolite Beta [14], 2D covalent triazine framework/g-C_3N_4 [15], carbon-based-nonprecious metal catalysts (NPMCs) [16], and Fluorographdiyne [17]. The covalent triazine framework in g-C_3N_4 enhanced the photocatalytic conversion of CO_2 to CO to give 151.1 μmol/(g.h) yield after 30 hours [15]. Zeolite is predominantly empolyed as support for CO_2 methanation. Synthesis of zeolite using various natural materials such as clay [20], bentonite [21], fly ash [22,23], and rice husk [23,24] as the source of alumina and silica affected the physicochemical properties and textural properties. The basicity, surface area and porosity of zeolite significantly affect the stability during CO_2 methanation [10,18,19]. However, the investigations of zeolite are limited to its effect as support without fully comprehending the inherent characteristics of zeolite on CO_2 reduction. Hussain et al. [14] synthesized metal-free fibrous zeolite

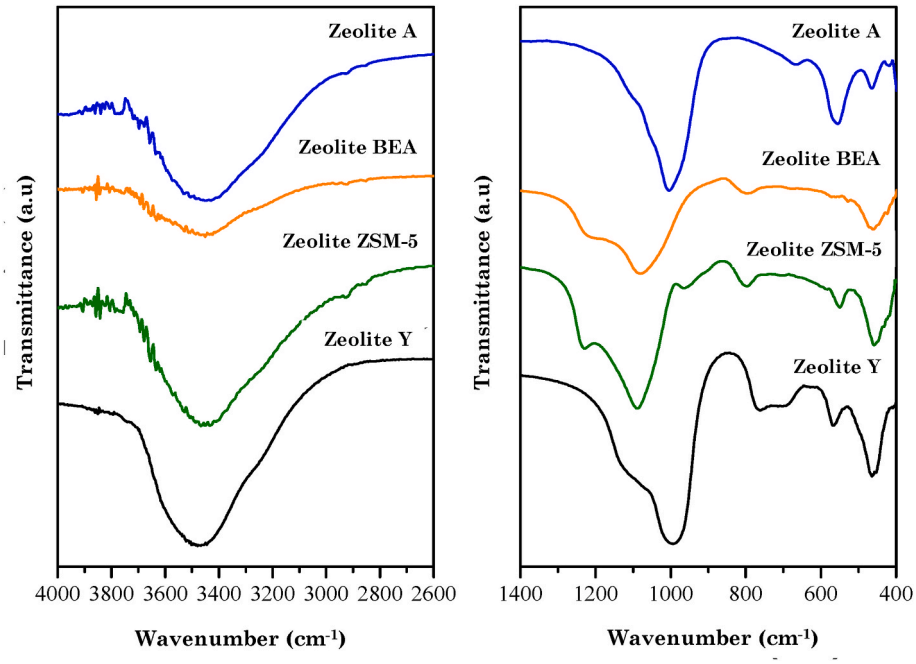

Fig. 2. FTIR analysis of zeolites.

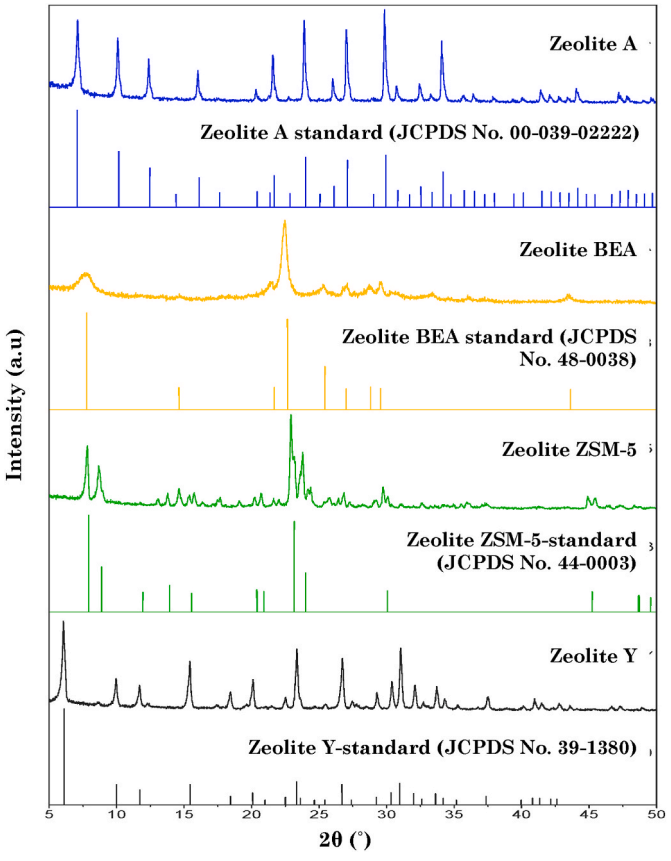

Fig. 3. XRD analysis of the zeolites.

(FS@SiO_2-BEA) with high basicity, oxygen vacancy, and large surface area for CO_2 methanation. The catalysts demonstrated 65 % CO_2 conversion and 61 % CH_4 selectivity, resulting in a space-time yield of 3.30 $g/g_{cat}/h$. Hence, we examined zeolite activity without any metal co-catalyst on CO_2 methanation. Four different zeolite frameworks (zeolite BEA, Y, ZSM-5, and A) were synthesized from Indonesian kaolin as silica and alumina sources. The correlation between basicity, acidity, the pore type (micropore-mesopore), and textural features were analyzed to understand their impact on the hydrogenation CO_2 to CH_4 and its stability over time (h).

2. Materials and methods

2.1. Materials

The silica colloidal (LUDOX®HS-40), hexadecyltrimethylammonium bromide (CTABr, $C_{19}H_{42}BrN$, ≥98 %), tetraethyl ammonium hydroxide (TEAOH, $C_4H_{13}NO$, 40 % in H_2O) were purchased from Sigma-Aldrich Company, pellets Natrium Hydroxide (NaOH, ≥99 %), and tetra propyl ammonium hydroxide (TPAOH, $C_{12}H_{29}NO$, 40 %) were purchased from Merck Company. Distilled water (H_2O) was used throughout the synthesis. Natural kaolin (57 wt% SiO_2 and 22 wt% Al_2O_3) from Bangka Belitung Island, Indonesia, was used as alternative alumina and silica sources.

2.2. Synthesis of zeolites

All zeolites were synthesized using the hydrothermal method, as shown in Fig. 1. Prior to synthesis, kaolin was calcined at 720 °C for 4 hours to form amorphous metakaolin [25]. The molar ratio of synthesized zeolites is shown in Table 1. The initial gel was produced by mixing all solutions outlined in Table 1 and referred to as solution 1. Distilled water was used to dissolve NaOH, which was then added to colloidal silica and homogenized using a magnetic stirrer until complete dissolution was achieved. Metakaolin was dissolved in distilled water, added to solution 1, and agitated for 30 minutes. The gel was aged before being transferred to the Teflon-line autoclave. Hydrothermal synthesis was conducted at a specific temperature and duration, as given in Table 1. The solid product was filtered, washed with H_2O, and dried overnight. The organic template was removed from ZSM-5 through calcination for 6 hours at 550 °C. For BEA, calcination was conducted at 550 °C for 1 hour under N_2 continuous flow, followed by 6 hours at 550 °C under air.

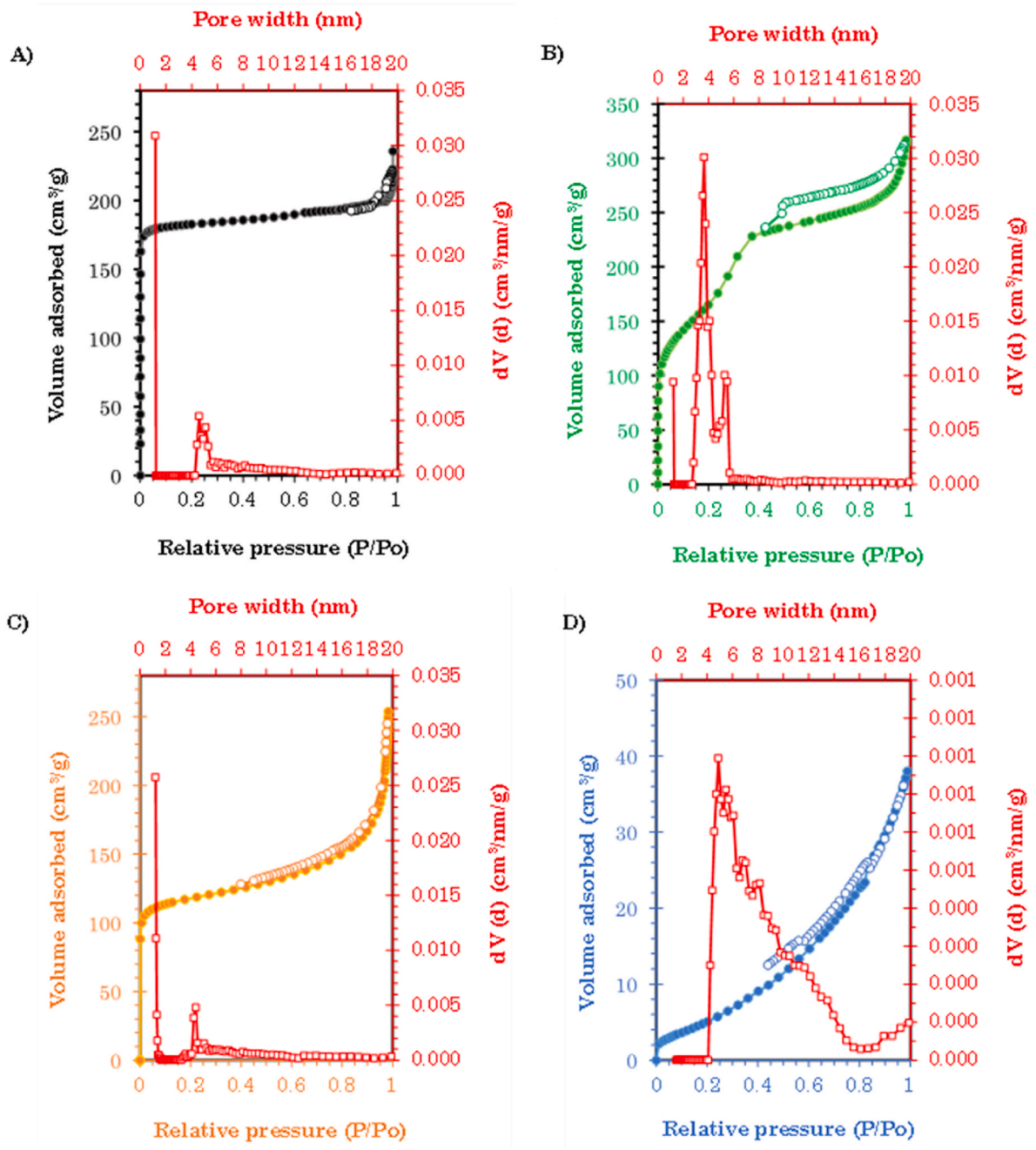

Fig. 4. The adsorption-desorption of N_2 and pore diameter size by NLDFT of zeolites a) Y, b) ZSM-5, c) BEA, and d) A.

2.3. Catalyst characterization techniques

The crystalline phase of zeolite was verified through X-ray diffraction (XRD) PHILIPS-binary Xpert MPD (Cu-Kα radiation with 2θ = 5–50°) using the diffractometer of 30 mA and 40 kV. The Beckman Coulter SA 3100 was used to analyze nitrogen adsorption-desorption. The zeolites were heated for 1 h at 90 °C and continued for a minimum of 4 h at 300 °C under vacuum. The Non-Localized Density Functional Theory (NLDFT) was used to determine the pore size distribution of zeolite. The adsorbed volume of N_2 was used to calculate V_{tot} (the total pore volume) at P/P_0 of 0.97. The micropore volume ($V_{microporous}$) was calculated using the t-plot method, and the mesopore volume ($V_{mesoporous}$) was calculated by subtracting V_{micro} from V_{tot}.

Temperature-programmed desorption using NH_3 as a probe molecule was used to determine the basicity, while CO_2 as a probe molecule determined acidity (NH_3/CO_2-TPD). A quartz tube was inserted with 50 mg of catalysts and reduced under the H_2 stream at 500 °C for 2 h. The reduced catalyst was flushed with N_2 and cooled to 50 °C. The catalyst was exposed to CO_2 flow for 30 min at 50 °C to allow adsorption and saturation. The excess adsorptive gas was purged with a He flow for 30 min before TPD measurement. After that, the temperature was increased to 650 °C at 10 °C min^{-1} under He, and the amount of CO_2 desorption was determined using a thermal conductivity detector (TCD). The basic properties of zeolite were determined using pyrrole as a probed molecule and analyzed using IR spectroscopy (Agilent Cary 640 FTIR spectrometer). The 30 mg zeolite shaped into self-supported wafer was inserted into a stainless steel cell with CaF_2 window. The zeolite was pretreated at 400 °C for 1 hour, cooled to room temperature and exposed to pyrrole vapour at 4 Torr for 15 minutes. The cell was outgassed to remove excess pyrrole before FTIR measurement. The spectra were

Table 2
Physicochemical properties of zeolites.

Sample	Si/Al[a]	Textural properties				Acidity		Basicity	
		S_{BET} (m^2 g^{-1})[a]	$V_{mesoporous}$ (cm^3 g^{-1})[b]	$V_{microporous}$ (cm^3 g^{-1})[c]	V_{tot} (cm^3 g^{-1})[c]	T_{desorp} NH_3 (°C)[d]	Uptake of NH_3 (mmol g^{-1})[d]	T_{desorp} CO_2 (°C)[e]	Uptake of CO_2 (mmol g^{-1})[e]
Y	1.24	415	0.17	0.28	0.45	153	1.48	270	0.04
								571	0.11
								723	0.87
ZSM-5	8.72	487	0.37	0.11	0.48	125	2.41	623	0.14
						500	0.15		
BEA	6.03	312	0.11	0.23	0.34	125	1.76	365	0.07
						493	0.19	457	0.05
						747	0.34	797	0.23
A	1.00	16	0.08	n.d.	0.08	130	1.41	146	0.24

[a] Ratio of Si/Al from EDX analysis.
[b] BET method for surface area measurement.
[c] t-plot method for pore volume measurement.
[d] Acidity from TPD-NH_3 analysis.
[e] Basicity from TPD-CO_2 analysis.

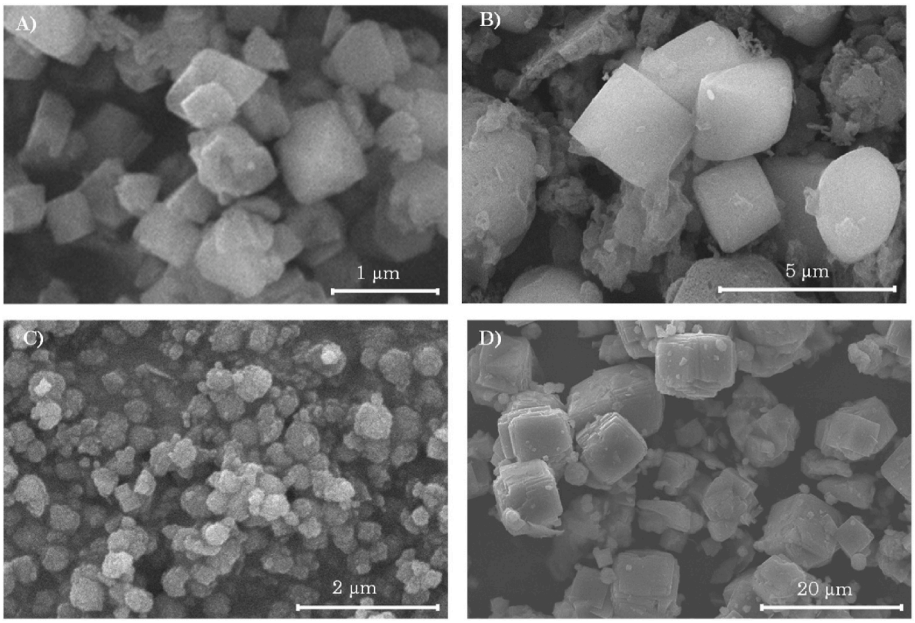

Fig. 5. SEM analysis of zeolites: A) zeolite Y, B) ZSM-5, C) BEA, and D) LTA.

obtained at 8 cm^{-1} spectral resolution.

2.4. Catalytic activity test

A fixed-bed quartz reactor with an interior diameter of 8 mm was used to conduct CO_2 methanation at a temperature of 200–500 °C under atmospheric pressure. The catalysts were sieved in the 20–40 μm fraction, weighed at 200 mg, and treated with an air stream at 550 °C for 1 hour, followed by a hydrogen stream for 4 hours. The catalysts were then cooled to the reaction temperature. Hydrogen and carbon dioxide at a 4:1 ratio were introduced into the reactor at 50,000 mL g^{-1} h^{-1} GHSV. The composition of the outlet gases was analyzed using an online gas chromatograph (7820 N Agilent Gas Chromatograph) with a moisture trap and TCD detector. The gas products were sampled after 1 hour of steady-state operation at each temperature. The following equations (1) and (2) were used to determine the selectivity of CH_4 and the conversion of CO_2:

$$X_{CO_2}(\%) = \left(M_{CH_4} + M_{CO}\right) / \left(M_{CO_2} + M_{CH_4} + M_{CO}\right) \times (100\%) \quad (1)$$

$$S_{CH_4}(\%) = \left(M_{CH_4}\right) / \left(M_{CH_4} + M_{CO}\right) \times (100\%) \quad (2)$$

where X_{CO2} was the conversion of CO_2 (%), SCH 4 was the selectivity of CH_4 and M was mol of gas methane (CH_4), carbon monoxide (CO), and carbon dioxide (CO_2) passing through the reactor.

3. Results and discussion

3.1. Characterization of catalysts

The functional groups and ring vibrations of zeolites were determined through FTIR analysis, as shown in Fig. 2. All the zeolites exhibited absorption peaks at 420-500 cm^{-1} as the vibration of *Si*–O and Al–O in tetrahedral TO_4 and at 3400-3500 cm^{-1} as the O–H stretching vibration of adsorbed water [25]. The zeolite Y exhibits TO_4 (T = Al or Si) and double ring vibrations D4R/D6R at 459 and 574 cm^{-1}. The symmetric vibrations of the OTO bond appeared at 698 and 786 cm^{-1} [26], while the symmetric stretching vibration of the TOT bond was observed at 1012 cm^{-1}. The ZSM-5 exhibits asymmetric stretching

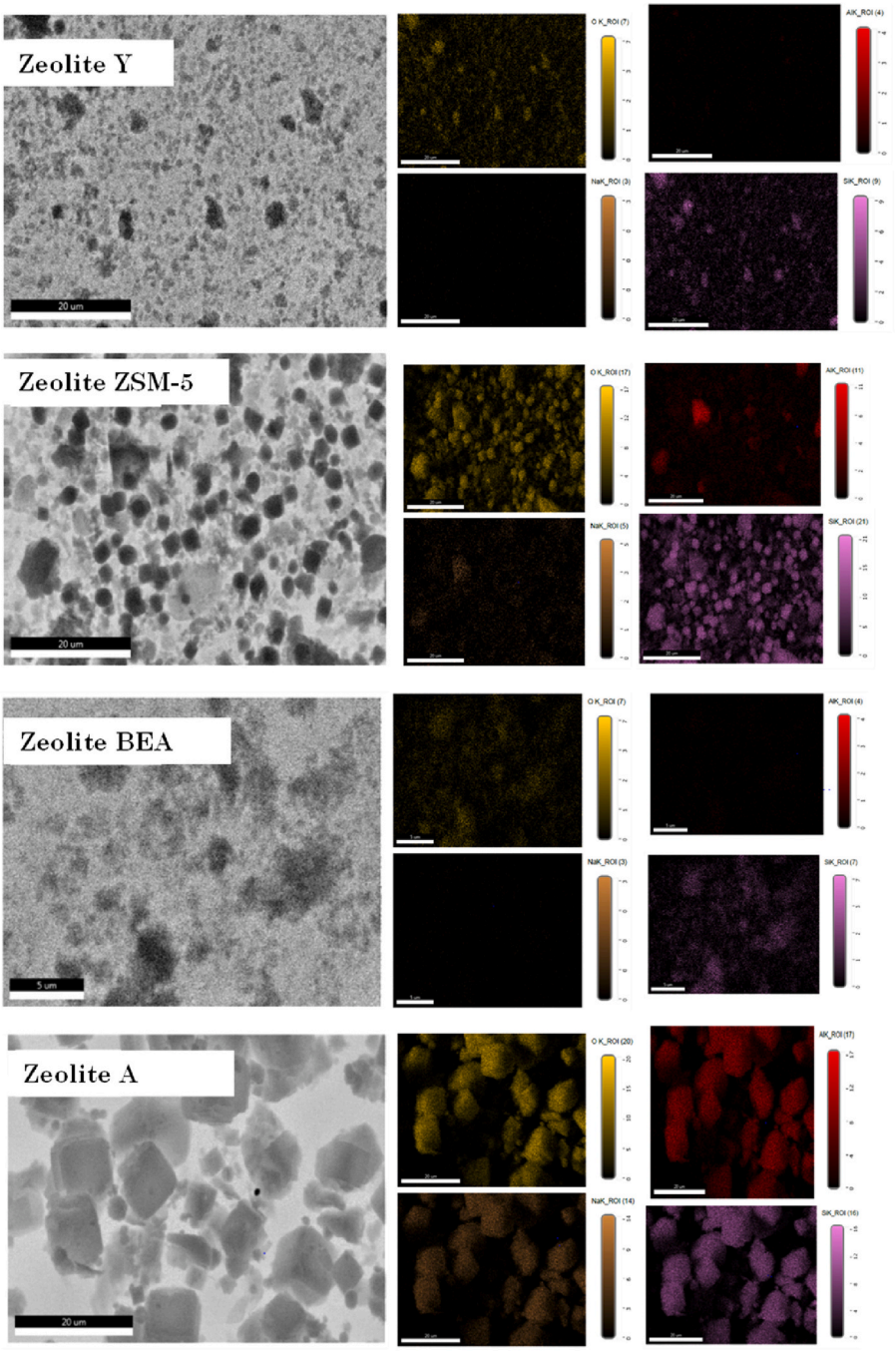

Fig. 6. EDX analysis of zeolites.

vibration of TO_4 at approximately 1100 cm^{-1} [27]. The peaks at 459 and 794 cm^{-1} represented the bending vibration of T-O for the sensitive internal tetrahedron structure [28]. The zeolite ZSM-5 structure is characterized by a framework-sensitive band at ~551 cm^{-1}, which suggests the presence of a typical five-ring unit. The asymmetric external stretching vibration for the TO_4 bond with the external vibration of the *Si–O–*Si oxygen bridge is represented by a peak at 1226 cm^{-1}. Furthermore, at 960 cm^{-1}, a shoulder peak indicates terminal silanol groups on the mesoporous walls. The FTIR spectra of BEA exhibit *Si–*O bond bending vibrations, TO_4 symmetric stretching vibrations, and TO_4 asymmetric stretching vibrations at 479, 791, and 1099 cm^{-1}, respectively. The absorption peak at 1099-1078 cm^{-1} suggests the presence of asymmetric stretching vibrations in TO_4, where T is Si or Al. The zeolite BEA formation is characterized by D6R double ring vibration at 568 cm^{-1}. The specific absorption peak of zeolite A was observed at 553 cm^{-1} indicating the external vibration [25].

X-ray diffraction (XRD) identifies the crystalline phase of zeolites, as depicted in Fig. 3. The synthesized zeolites exhibited distinctive peaks aligned with the JCPDS standard data for each zeolite. The characteristic peaks of kaolin at $2\theta = 12°$, 20°–25°, and 35°–40°, as well as the broad peak of amorphous metakaolin, were absent, indicating complete conversion of metakaolin into zeolite. The diffraction pattern of zeolite Y was observed at 2θ = 6.15°; 10.05°; 11.79°; 15.53°; 18.52°; 23.46°; 26.82° and 31.13° [29]. Diffraction peaks in zeolite ZSM-5 were detected at 2θ = 7.8; 8.7; 23.0; 23.8; and 24.0° [30]. The diffraction peak of zeolite BEA appeared at 2θ = 7.7°, 21.4°, and 42.5°, which correlate to the lattice parameters of (101), (004), (201), (106), and (311) planes [14]. Zeolite A exhibits peaks at 2θ = 7.2, 10.2, 12.5, 16.1,

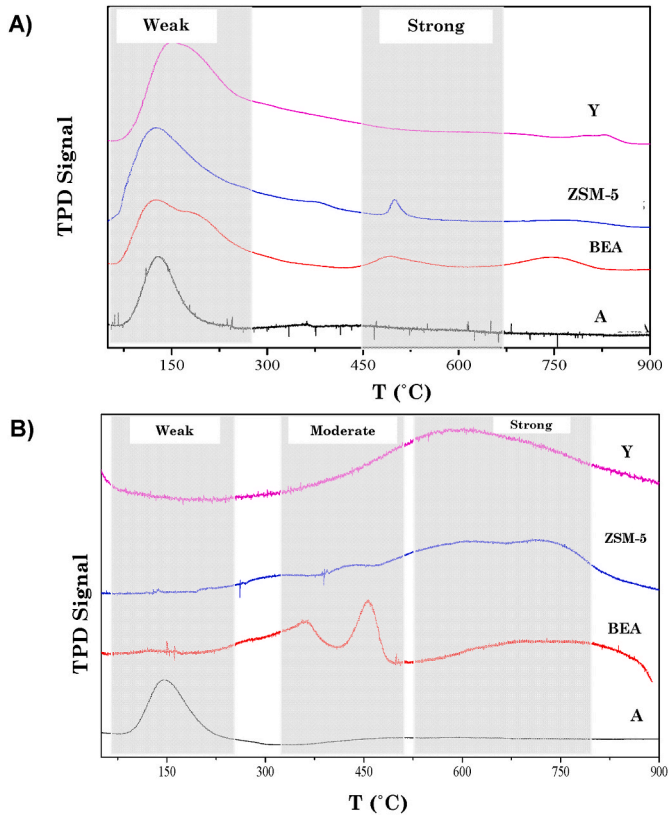

Fig. 7. a) NH_3-TPD and b) CO_2-TPD analysis of zeolites.

21.6, 24, 26.1, 27.1, 29.9, and 34.2° [19].

Fig. 4 shows the N_2 adsorption-desorption analysis of the zeolite to establish its textural properties. The results indicate that zeolites exhibit several adsorption-desorption isotherms, suggesting diverse porosities. Zeolite Y and BEA exhibit a type I isotherm characterized by significant nitrogen gas adsorption at a very low relative pressure ($P/Po < 0.1$). The horizontal N_2 uptake from a low to high P/P_o indicates that the amount of gas adsorbed achieves a steady state, a typical attribute of the type I isotherm (microporous solid) according to IUPAC classification. The ZSM-5 has a type IV isotherm profile, indicative of mesoporous materials. Despite being classed as a microporous material, zeolite A exhibits a type II isotherm in N_2 adsorption-desorption studies due to its smaller pore width than nitrogen molecule size. The zeolite pore size using NLDFT methods for zeolite BEA, Y, and A ranges from 1 to 1.5 nm, whereas ZSM-5 ranges from 4 to 5 nm, as shown in Fig. 4c. Based on Table 2, the surface areas of zeolite ZSM-5, Y, BEA, and A are 487, 415, 312 and 16 m^2/g, respectively. Zeolite ZSM-5 has the highest V_{total} and S_{BET} because of the formation of micropores and meso-sized pores in the structure.

The morphology of zeolites synthesized from kaolin was examined using scanning electron microscopy as depicted in Fig. 5. The zeolite Y exhibits a noticeable octahedral morphology. Zeolite A exhibited a cuboid shape [31]. However, zeolite ZSM-5 lacks a hexagonal structure, while zeolite BEA lacks an octahedral structure due to particle aggregation [25].

The elemental composition of the zeolite catalyst is determined using EDX analysis. The results of the constituent element composition are summarized in Table 2. Fig. 6 illustrates the elemental mapping of Na, Si, Al and O on the zeolites. The Si/Al ratios of zeolite Y, ZSM-5, BEA, and A were calculated based on Si and Al composition, which are 1.24, 23.23, 9.71, and 1.00, respectively. The Si/Al corresponds to the classification of zeolites in which FAU (Y) and LTA (A) zeolites possess a Si/Al ratio of less than 2. Zeolite Y was reported to have Si/Al ratio of 1.61, while zeolite A has a Si/Al ratio of 1 [32]. Zeolite BEA and ZSM-5 have higher Si/Al ratios >5 [33].

The TPD technique characterizes and quantifies acid/base sites in zeolites. The NH_3 and CO_2 molecules are employed as probe molecules for acid and base measurements in TPD. Fig. 7a displays the NH_3-TPD of zeolite, revealing two distinct desorption peaks occurring at temperatures ranging from 50 to 200 °C and 450–500 °C. The desorption of NH_3 at low temperatures on all zeolites indicates weak acidic sites due to the physical adsorption of NH_3 on the silanol groups present on the zeolite surface [34]. Both BEA and ZSM-5 exhibit desorption peaks at high temperatures (450–500 °C), suggesting chemisorbed NH_3. ZSM-5 and BEA zeolites had the most significant amount of acid sites, with NH_3 adsorption values of 2.56 and 2.19 mmol/g, respectively (Table 2). The high total acidity of ZSM-5 might be due to the accessibility of ammonia molecules to diffuse into mesopores. The NH_3 cross-sectional area is 0.141 nm^2, which can diffuse to the ZSM-5 zeolite mesoporous and micropores. Moreover, the elimination of the template during calcination leads to the emergence of silanol groups on the zeolite surface, further increasing the acidity. The acidity in zeolite is also directly related to the Si/Al ratio. According to the SEM-EDX data, BEA and ZSM-5 have Si/Al ratios of 8 and 6, respectively, which are higher than

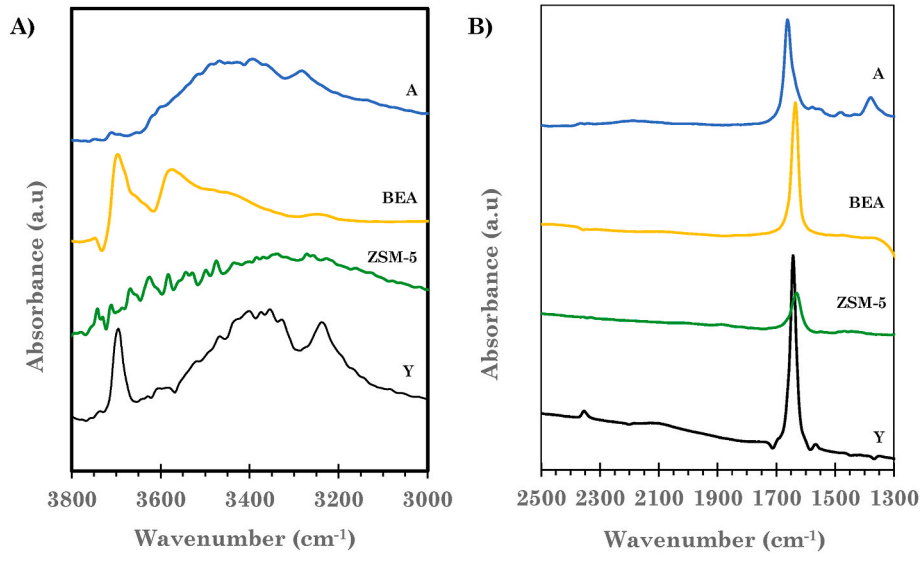

Fig. 8. Pyrrole adsorption of zeolites at a) 3800–3000 and b) 2500-1300 cm^{-1}.

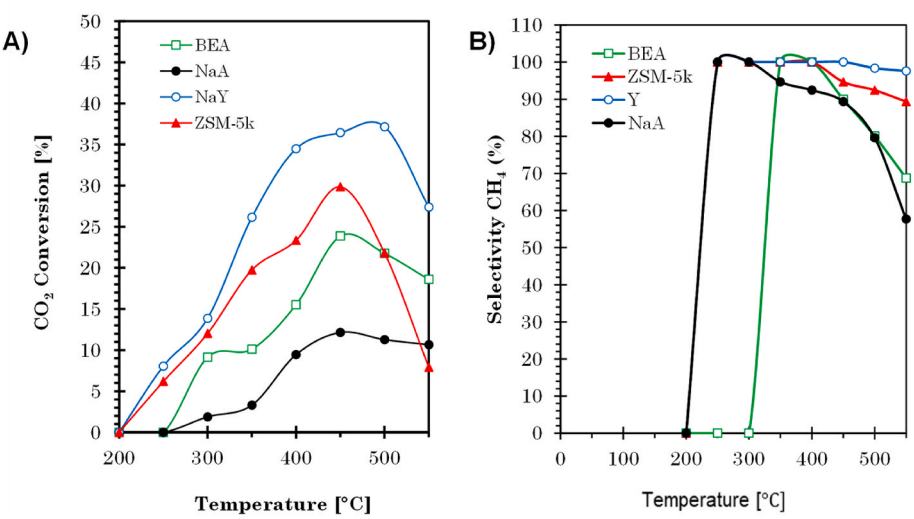

Fig. 9. a) CO_2 conversion and b) CH_4 selectivity of zeolites.

Table 3
Catalyst comparison for CO_2 methanation at 400 °C.

Materials	Source	S_{BET} (cm^2/g)	V_{pore} (cm^3/g)	XCO_2 (%)	Stability test (h)	References
NaY	Kaolin	415	0.45	36.64	20	This study
Na-ZSM-5	Kaolin	487	0.48	29.85	30	This study
Ni/BEA	–	516	0.46	40	–	[43]
Ni/ZSM-5	–	333	0.15	50	–	
Ni-4A	–	12	0.02	60	–	
Ni-5A	–	367	0.19	72	–	
Ni-13X	–	377	0.20	70	–	
Zeolite A	Kaolin	–	–	~0	–	[44]
Ni/A	Kaolin	–	–	40	–	
Ni–Ce	Kaolin	23.83	–	47.8	50	[45]
Ni–Ce	Halloysite	41	0.19	40	50	[46]
NiCe-Activated Carbon	Cork Waste	535	0.33	73	24	[47]
Ni/CGLTA-5A	Coal gangue	167.5	0.118	70	50	[48]

zeolite Y and A. Therefore, high acidity further enhanced the overall quantity of NH_3 adsorption.

Fig. 7b displays the analysis of base strength conducted using CO_2-TPD. Multiple peaks of CO_2 desorption were observed at different temperatures: 100–200 °C, 200–500 °C, and 500–600 °C, with variable intensities. The desorption peak observed at a temperature of 150 °C indicates the presence of weakly basic sites, which can be attributed to the physical adsorption of CO_2 on zeolite A. At 450 °C, the peak indicates the presence of medium basicity in BEA. Peaks above 600 °C in zeolite Y and ZSM-5 suggest a high basicity [25].

The basicity in the N–H stretching area on zeolite can be determined by analyzing the FTIR adsorption of pyrrole (C_4H_4NH), as shown in Fig. 8. Pyrrole is a molecule that exhibits amphoteric properties, meaning it may interact with both Lewis acidic cations through aromatic π-electron interactions and with Lewis basic oxygen in the silicate framework through hydrogen bonding facilitated by the N–H group. The zeolites show adsorption peaks in the range of 1700-1500 cm^{-1}, corresponding to the bending of C═C bonds, as the pyrrole structure. Moreover, the peak at 3800 cm^{-1} in zeolite Y and BEA corresponds to isolated Si–OH species [35]. Additionally, there is a larger absorption band at around 3530 cm^{-1}, which is caused by H-bonded Si–OH interacting with the pyrrole N–H band in the gas phase. In addition, the broad band, at ~3475-3200 cm^{-1} is assigned to the N–H stretching vibrations of chemisorbed pyrrole that interact with the basic sites of framework oxygens in zeolite Y [36]. The pyrrole characteristics, which act as H-donors, allowed the formation of C_4H_4NH–O bridges with the basic oxygen [37]. Therefore, this result corroborates the CO_2-TPD findings, showing that zeolite Y possesses more basic sites than other zeolites.

3.2. *Catalytic conversion of CO_2 methanation*

The CO_2 conversion of all metal-free zeolite catalysts increases as the temperature rises from 200 to 400 °C (Fig. 9). However, the conversion decreases above 450 °C due to thermodynamic constraints [38]. In the order of Y > ZSM-5 > BEA > A, zeolite Y exhibits the maximum catalytic activity among the other catalysts with approximately 36.64 % conversion at 450 °C and 100 % selectivity to methane (Table 3). The zeolites examined in this work exhibit higher CO_2 conversion rates than zeolite A without any metal co-catalyst, as reported by Son et al. [44]. Zeolite Y achieved considerably more CO_2 conversion than ZSM-5 at 300 °C, up to 1.5 times higher, presumably due to the high quantity of base sites in zeolite Y. Surface hydroxyl groups generate weak base sites, while surface oxygen generates medium and strong base sites [40]. CO_2 methanation was reported to occur on medium-strength basic sites [39]. The electron pairs from surface oxygen facilitate the production of bidentate carbonate, the primary intermediate in CO_2 methanation [25]. However, at temperatures above >450 °C, all zeolites exhibited reduced methane selectivity due to CO formation from methane steam reforming

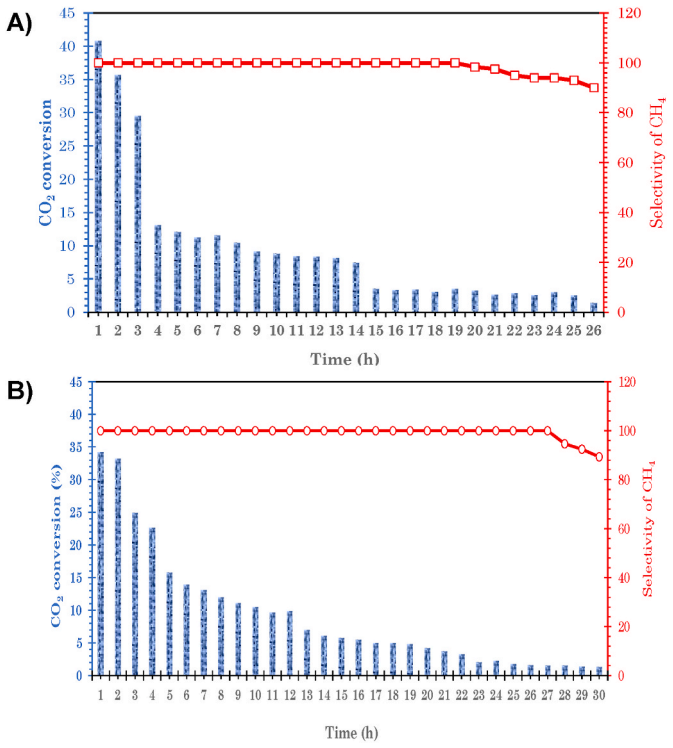

Fig. 10. Stability test of CO_2 conversion and CH_4 selectivity on a) zeolite Y and b) zeolite ZSM-5 at 400 °C.

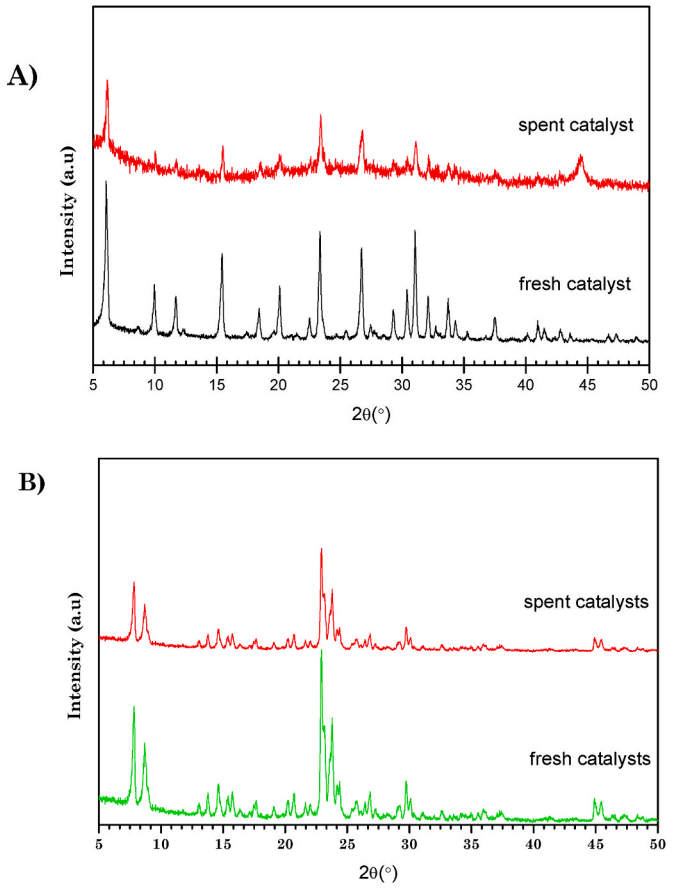

Fig. 11. XRD analysis of spent catalyst of a) zeolite Y and b) zeolite ZSM-5.

(MSR) or reverse water gas shift reaction (RWGS) (Equations (3) and (4)):

Methane steam reforming (SMR)

$$CH_{4(g)} + H_2O_{(l)} \rightleftharpoons CO_{(g)} + 3H_{2(g)} \ (\Delta H^{o}_{298} = 205{,}9 \text{ kJ/mol}) \quad (3)$$

Reverse water gas shift reaction (RWGS)

$$CO_{2(g)} + H_{2(g)} \rightleftharpoons CO_{(g)} + 2H_2O_{(g)} \ (\Delta H^{o}_{298} = 41 \text{ kJ/mol}) \quad (4)$$

In high-temperature heterogeneous catalytic processes, catalysts often undergo deactivation due to metal sintering and coke deposition [41]. A stability test was performed on the zeolite Y and zeolite ZSM-5 catalysts for 30 hours at 400 °C. Fig. 10 shows CO_2 conversion and methane selectivity at 400 °C for 30 hours. The initial conversion was determined at 36.6 % for zeolite Y, and 34.10 % for zeolite ZSM-5. Interestingly, the selectivity of all catalysts in producing methane remained constant for 30 h, with only a slight decrease of 6–10 %. The CH_4 selectivity remained consistent, staying close to 95 % throughout the reaction. After 26 hours, the efficiency and durability of zeolite Y as a microporous material experienced contineous reduction in CO_2 conversion to reach 4 % at 26h. ZSM-5 zeolite, with mesoporous properties, also exhibited reduced conversion to 3 % at 30 hours. During a long catalytic reaction, a slow decline in catalytic performance may have resulted from structural alterations, poisoning, overheating, or the accumulation of foreign substances, such as coke [42]. The coke formation, $C_{(s)}$ is due to the following reaction (Equations (5)–(8)):

Boudouard reaction:

$$2\,CO(g) \leftrightarrow C(s) + CO_2(g) \ \Delta H_{298\ K} = -172{,}4 \text{ kJ/mol}^{-1} \quad (5)$$

Methane *cracking*:

$$CH_4(g) \leftrightarrow C(s) + 2H_2(g) \ \Delta H_{298\ K} = 74{,}6 \text{ kJ/mol}^{-1} \quad (6)$$

CO_2 reduction:

$$CO_2(g) + 2H_2(g) \leftrightarrow C(s) + 2H_2O(g) \ \Delta H_{298K} = -90{,}1 \text{ kJ/mol}^{-1} \quad (7)$$

CO reduction:

$$CO(g) + H_2(g) \leftrightarrow C(s) + H_2O(g) \ \Delta H_{298K} = -131.3 \text{ kJ/mol}^{-1} \quad (8)$$

The stability of the catalyst was verified using X-ray diffraction (XRD) analysis of the spent catalyst, as shown in Fig. 11. Zeolite Y exhibits a decline in peak intensity, indicating the disintegration of the crystalline into amorphous structures after long CO_2 methanation. However, the spent zeolite Y still showed the specific angles: 2θ = ~6.15; 10.05; 11.79; 15.53; 18.52; 23.46; 26.82; 31.13° [29]. There is no significant alteration in the zeolite ZSM-5 framework after 30h reaction, suggesting that ZSM-5 possesses good thermal stability. The spent ZSM-5 peaks were observed at $2\theta = 7.8$; 8.7; 23.0; 23.8; and 24.0° [30]. The good stability of zeolite has also been reported by Bahraminia et al. [48] that the peaks associated with the LTA phase remain detectable in the used catalyst, suggesting that the zeolite maintains its stability under operational conditions.

4. Conclusions

Zeolite Y, BEA, ZSM-5, and A from Indonesian kaolin were synthesized using the hydrothermal method and investigated as catalysts for CO_2 methanation. The textural properties, acidity, type of pore, and basicity of zeolites were determined to understand the effect of CO_2 methanation. The surface area of zeolite Y, BEA, ZSM-5, and A are 415, 312, 487, and 16 cm^2/g, respectively. The CO_2 methanation results exhibited good catalytic performance of zeolite Y, BEA, ZSM-5, and A without the addition of metal co-catalysts, reaching 36.64 %, 23.86 %, 29.85 %, and 12.15 % conversion, respectively, at 400 °C with 100 % CH_4 selectivity. The highest CO_2 methanation activity of zeolite Y was due to the presence of moderate basicity at 1.02 mmol/g compared to

BEA, ZSM-5, and A at 0.35 mmol/g, 0.14 mmol/g, and 0.24 mmol/g, respectively. CO_2 methanation is predominantly activated by the basic sites rather than the acid sites. The electron donations from basic oxygen initiate the formation of bidentate carbonate intermediates. However, the stability of the catalysts depends on the pore sizes. The mesoporous structure in ZSM-5 improves the mass transfer and prevents coke deposition, maintaining the crystallinity up to 30h reaction.

CRediT authorship contribution statement

Novia Amalia Sholeha: Writing – review & editing, Writing – original draft, Methodology, Investigation, Data curation, Conceptualization. **Bintang Dewanto:** Methodology, Data curation. **Stella Jovita:** Writing – review & editing, Data curation. **Reva Edra Nugraha:** Writing – review & editing. **Yun Hin Taufiq-Yap:** Writing – review & editing, Data curation. **Maria Ulfa:** Writing – review & editing, Resources. **Anees Ameera Fauzi:** Writing – review & editing, Visualization. **Aishah Abdul Jalil:** Resources, Writing – review & editing. **Hasliza Bahruji:** Writing – review & editing. **Didik Prasetyoko:** Writing – review & editing, Supervision, Resources, Methodology.

Declaration of competing interest

The authors declare that they have no known competing financial interests or personal relationships that could have appeared to influence the work reported in this paper.

Data availability

Data will be made available on request.

Acknowledgments

The author would like to acknowledge Institut Pertanian Bogor thoroughly Riset Kolaborasi Nasional (RI-NA) Scheme No. 523/IT3.D10/PT.01.03/P/B/2023 to Novia Amalia Sholeha. Additionally, the authors would like to express their gratitude to Dr. Nurul Asikin Mijan for their contribution to this research and for their continued collaboration.

References

[1] A.A.M. Abahussain, A.S. Al-fatesh, Y.B. Rajput, A.I. Osman, S.B. Alreshaidan, H. Ahmed, A.H. Fakeeha, A.S. Al-awadi, R.A. El-salamony, R. Kumar, Impact of Sr addition on z irconia – alumina-supported Ni catalyst for COx - free CH4 production via CO2 methanation, ACS Omega 9 (2024) 9309–9320, https://doi.org/10.1021/acsomega.3c08536.

[2] I. Martínez-lopez, J.C. Martínez-fuentes, J. Bueno-ferrer, A. Davo-Quinonero, E. Guillen-bas, E. Bailon-garcia, D. Lozano-castell, A. Bueno-López, Structural design and particle size examination on NiO-CeO2 catalysts supported on 3D-printed carbon monoliths for CO2 methanation, J. CO2 Util. 81 (2024) 102733, https://doi.org/10.1016/j.jcou.2024.102733.

[3] O. V Netskina, K.A. Dmitruk, O.I. Mazina, A.A. Paletsky, S.A. Mukha, I.P. Prosvirin, A.A. Pochtar, O.A. Bulavchenko, A.G. Shmakov, J. V Veselovskaya, O. V Komova, CO2 methanation: solvent-free synthesis of nickel-containing catalysts from complexes with ethylenediamine, Materials 16 (2023) 2616.

[4] L.A. Sani, H. Bai, Z. Xu, L. Fu, Y. Sun, X. Huang, H. Gao, X. Liu, D. Bai, Z. Zhang, F. Su, J. Liu, G. Xu, Optimized combustion temperature in the facile synthesis of Ni/Al2O3 catalyst for CO2 methanation, J. CO2 Util. 80 (2024) 102678, https://doi.org/10.1016/j.jcou.2024.102678.

[5] Y. Choi, J.J. Jang, S. Hwang, M.W. Seo, D. Lee, S.K. Jeong, H.-J. Ryu, S.-A. Choi, B. Hwang, H. Nam, Optimizing heat transfer rate for efficient CO2-to-chemical conversion in CO2 methanation and CO2 hydrogenation reactions, J. CO2 Util. 81 (2024) 102730, https://doi.org/10.1016/j.jcou.2024.102730.

[6] A. Rizzetto, M. Piumetti, R. Pirone, E. Sartoretti, S. Bensaid, Study of ceria-composite materials for high-temperature CO2 capture and their ruthenium functionalization for methane production, Catal. Today 429 (2024) 114478, https://doi.org/10.1016/j.cattod.2023.114478.

[7] A. Dastbaz, J. Karimi-sabet, Y. Amini, M.A. Moosavian, A comprehensive study on the kinetics and isotherms of D2/H2 adsorptive separation using pure and composite Cu-BDC-NH2 MOFs at 77 K, Int. J. Hydrogen Energy 61 (2024) 893–900, https://doi.org/10.1016/j.ijhydene.2024.02.366.

[8] F.M. Baena-moreno, N. Cid-castillo, H. Arellano-garcía, T.R. Reina, Towards emission free steel manufacturing – exploring the advantages of a CO2 methanation unit to minimize CO2 emissions, Sci. Total Environ. 781 (2021) 146776, https://doi.org/10.1016/j.scitotenv.2021.146776.

[9] L. Wang, Y. Qi, Z. Yang, H. Wu, J. Liu, Y. Tang, F. Wang, Pt nanoparticles supported LaCoO3 as highly efficient catalysts for photo-thermal catalytic CO2 methanation, Green Energy Resour. 1 (2023) 100036, https://doi.org/10.1016/j.gerr.2023.100036.

[10] N.A. Sholeha, H. Holilah, H. Bahruji, A. Ayub, N. Widiastuti, R. Ediati, A. Abdul, M. Ulfa, N. Masruchin, R. Edra, D. Prasetyoko, Recent trend of metal promoter role for CO2 hydrogenation to C1 and C2+ products, South Afr. J. Chem. Eng. 44 (2023) 14–30, https://doi.org/10.1016/j.sajce.2023.01.002.

[11] H. Fu, S. Sun, H. Lian, Enhanced low-temperature CO2 methanation over Ni/ZrO2-Al2O3 catalyst: effect of Al addition on catalytic performance and reaction mechanism, J. CO2 Util. 69 (2023) 102415, https://doi.org/10.1016/j.jcou.2023.102415.

[12] J. He, X. Wang, S. Jin, Z. Qing, M. Zhu, 2D metal-free heterostructure of covalent triazine framework/g-C3N4 for enhanced photocatalytic CO2 reduction with high selectivity, Chin. J. Catal. 43 (2022) 1306–1315, https://doi.org/10.1016/S1872-2067(21)63936-0.

[13] H. Shen, T. Peppel, J. Strunk, Z. Sun, Photocatalytic reduction of CO2 by metal-free-based materials recent advances and future, Sol. RRL 4 (2020) 1900546.

[14] I. Hussain, A.A. Jalil, S.M. Izan, M.S. Azami, K. Kidam, N. Ainirazali, A. Ripin, Thermodynamic and experimental explorations of CO2 methanation over highly active metal-free fibrous silica-beta zeolite (FS@SiO2-BEA) of innovative morphology, Chem. Eng. Sci. 229 (2021) 116015, https://doi.org/10.1016/j.ces.2020.116015.

[15] X. Liu, P.V. Kumar, Q. Chen, L. Zhao, F. Ye, X. Ma, D. Liu, X. Chen, L. Dai, C. Hu, Carbon nanotubes with fluorine-rich surface as metal-free electrocatalyst for effective synthesis of urea from nitrate and CO2, Appl. Catal. B Environ. 316 (2022) 121618, https://doi.org/10.1016/j.apcatb.2022.121618.

[16] S. Zhao, D.-W. Wang, R. Amal, L. Dai, Carbon-based metal-free catalysts for key reactions involved in energy conversion and storage, Adv. Mater. 31 (2019) 1801526, https://doi.org/10.1002/adma.201801526.

[17] C. Xing, Y. Xue, B. Huang, H. Yu, L. Hui, Y. Fang, Y. Liu, Y. Zhao, Z. Li, Y. Li, Fluorographdiyne: a metal-free catalyst for applications in water reduction and oxidation, Angew. Chem. Int. Ed. 58 (2019) 13897–13903.

[18] M. Sedighi, M. Mohammadi, CO2 hydrogenation to light olefins over Cu-CeO2/SAPO-34 catalysts: product distribution and optimization, J. CO2 Util. 35 (2020) 236–244, https://doi.org/10.1016/j.jcou.2019.10.002.

[19] L. Wei, N. Kumar, W. Haije, J. Peltonen, M. Peurla, H. Grénman, W. de Jong, Can bi-functional nickel modified 13X and 5A zeolite catalysts for CO2 methanation be improved by introducing ruthenium? Mol. Catal. 494 (2020) 111115 https://doi.org/10.1016/j.mcat.2020.111115.

[20] S.O. Otieno, F.O. Kengara, J.C. Kemmegne-Mbouguen, H.W. Langmi, C.B. O. Kowenje, R. Mokaya, The effects of metakaolinization and fused-metakaolinization on zeolites synthesized from quartz rich natural clays, Microporous Mesoporous Mater. 290 (2019) 109668, https://doi.org/10.1016/j.micromeso.2019.109668.

[21] M.S. Hosseini Hashemi, F. Eslami, R. Karimzadeh, Organic contaminants removal from industrial wastewater by CTAB treated synthetic zeolite Y, J. Environ. Manag. 233 (2019) 785–792, https://doi.org/10.1016/j.jenvman.2018.10.003.

[22] N. Czuma, K. Zar, M. Motak, M.E. Gálvez, P. Da Costa, Ni/zeolite X derived from fly ash as catalysts for CO2 methanation, Fuel 267 (2020) 117139, https://doi.org/10.1016/j.fuel.2020.117139.

[23] A. Khaleque, M.M. Alam, M. Hoque, S. Mondal, J. Bin Haider, B. Xu, M.A.H. Johir, A.K. Karmakar, J.L. Zhou, M.B. Ahmed, M.A. Moni, Zeolite synthesis from low-cost materials and environmental applications: a review, Environ. Adv. 2 (2020) 100019, https://doi.org/10.1016/j.envadv.2020.100019.

[24] Y. Cui, J. Qiu, B. Chen, L. Xu, M. Chen, C. Wu, G. Cheng, B. Yang, N. Wang, X. Hu, CO2 methanation over Ni/ZSM-5 catalysts: the effects of support morphology and La2O3 modification, Fuel 324 (2022) 124679, https://doi.org/10.1016/j.fuel.2022.124679.

[25] N.A. Sholeha, S. Mohamad, H. Bahruji, D. Prasetyoko, N. Widiastuti, N.A. Abdul Fatah, A.A. Jalil, Y.H. Taufiq-Yap, Enhanced CO2 methanation at mild temperature on Ni/zeolite from kaolin: effect of metal-support interface, RSC Adv. 11 (2021) 16376–16387, https://doi.org/10.1039/d1ra01014j.

[26] N.A. Sholeha, L. Jannah, H.N. Rohma, N. Widiastuti, D. Prasetyoko, A.A. Jalil, H. Bahruji, Synthesis of zeolite NaY from dealuminated metakaolin as Ni support for CO2 hydrogenation to methane, Clay Clay Miner. 68 (2020) 513–523, https://doi.org/10.1007/s42860-020-00089-3.

[27] X. Guo, A. Traitangwong, M. Hu, C. Zuo, V. Meeyoo, Z. Peng, C. Li, Carbon dioxide methanation over nickel-based catalysts supported on various mesoporous material, Energy Fuel. 32 (2018) 3681–3689, https://doi.org/10.1021/acs.energyfuels.7b03826.

[28] D. Xu, Y. Wang, M. Ding, X. Hong, G. Liu, S. Chi, E. Tsang, Advances in higher alcohol synthesis from CO2 hydrogenation, Chem 7 (2021) 849–881, https://doi.org/10.1016/j.chempr.2020.10.019.

[29] Y. He, S. Tang, S. Yin, S. Li, Research progress on green synthesis of various high-purity zeolites from natural material-kaolin, J. Clean. Prod. 306 (2021) 127248, https://doi.org/10.1016/j.jclepro.2021.127248.

[30] R. Liu, D. Leshchev, E. Stavitski, M. Juneau, J.N. Agwara, M.D. Porosoff, Selective hydrogenation of CO2 and CO over potassium promoted Co/ZSM-5, Appl. Catal. B Environ. 284 (2021) 119787, https://doi.org/10.1016/j.apcatb.2020.119787.

[31] N.A. Sholeha, T.U.P. Sujarnoko, N.R.A.S. Eryasaputri, O. Farobie, N. Masruchin, I. Susanti, R. Wijiyanti, N.S.B. Hassan, R.M. Iqbal, N. Widiastuti, In-situ growth of

zeolite-A in the fiber surface for methane adsorption, in: E3S Web Conf., 2023 02018.
[32] M. Wang, D. Xu, H. Ma, B. Li, A. Howard, Synthesis of NaA zeolite from foundry dust and its adsorption capacity of ammonia, J. Environ. Manag. 331 (2023) 117297, https://doi.org/10.1016/j.jenvman.2023.117297.
[33] W. Gac, W. Zawadzki, G. Słowik, M. Kuśmierz, S. Dzwigaj, The state of BEA zeolite supported nickel catalysts in CO2 methanation reaction, Appl. Surf. Sci. 564 (2021) 150421, https://doi.org/10.1016/j.apsusc.2021.150421.
[34] Z. Taherian, A. Khataee, Y. Orooji, Promoted nickel-based catalysts on modified mesoporous silica support: the role of yttria and magnesia on CO2 methanation, Microporous Mesoporous Mater. 306 (2020) 110455, https://doi.org/10.1016/j.micromeso.2020.110455.
[35] F. Zhao, S. Chen, H. Xiang, T. Gao, D. Wang, D. Wei, M. Sillanpaa, Y. Ke, C. Tang, Selectively capacitive recovery of rare earth elements from aqueous solution onto Lewis base sites of pyrrolic-N doped activated carbon electrodes, Carbohydr. Polym. 197 (2022) 282–291, https://doi.org/10.1016/j.carbon.2022.06.033.
[36] F. Maleki, G. Pacchioni, Characterization of acid and basic sites on zirconia surfaces and nanoparticles by adsorbed probe molecules: a theoretical study, Top. Catal. 63 (2020) 1717–1730, https://doi.org/10.1007/s11244-020-01328-6.
[37] X. Wu, X. Sang, Z. Li, D. Tao, Study on physicochemical properties and basicity of carbanion-functionalized ionic liquids, J. Mol. Liq. 312 (2020) 113405, https://doi.org/10.1016/j.molliq.2020.113405.
[38] L. Xu, X. Wen, M. Chen, C. Lv, Y. Cui, X. Wu, C. Wu, Z. Miao, X. Hu, Highly dispersed Ni-La catalysts over mesoporous nanosponge MFI zeolite for low-temperature CO2 methanation: synergistic effect between mesoporous and microporous channels, J. Ind. Eng. Chem. 100 (2021) 159–173, https://doi.org/10.1016/j.jiec.2021.05.026.
[39] C. Lv, L. Xu, M. Chen, Y. Cui, X. Wen, C.e. Wu, B. Yang, F. Wang, Z. Miao, X. Hu, Q. Shou, Constructing highly dispersed Ni based catalysts supported on fibrous silica nanosphere for low-temperature CO2 methanation, Fuel 278 (2020) 118333, https://doi.org/10.1016/j.fuel.2020.118333.
[40] J. Guilera, J. Valle, A. Alarcón, J.A. Díaz, T. Andreu, Metal-oxide promoted Ni/Al2O3 as CO2 methanation micro-size catalysts, J. CO2 Util. 30 (2019) 11–17, https://doi.org/10.1016/j.jcou.2019.01.003.
[41] K. Li, X. Chang, C. Pei, X. Li, S. Chen, X. Zhang, S. Assabumrungrat, Z.J. Zhao, L. Zeng, J. Gong, Ordered mesoporous Ni/La2O3 catalysts with interfacial synergism towards CO2 activation in dry reforming of methane, Appl. Catal. B Environ. 259 (2019) 118092, https://doi.org/10.1016/j.apcatb.2019.118092.
[42] A. Gamal, M. Tang, A.K. Bhakta, Y. Snoussi, A.M. Khalil, K. Jlassi, M.M. Chehimi, A.M.A. Ali, CO2 methanation using sugarcane bagasse biochar/nickel sustainable catalysts, Mater. Today Sustain. 25 (2024) 100627, https://doi.org/10.1016/j.mtsust.2023.100627.
[43] P. Yan, H. Peng, X. Wu, H. Rabiee, Y. Weng, M. Konarova, J. Vogrin, A. Rozhkovskaya, Z. Zhu, Impact of varied zeolite materials on nickel catalysts in CO2 methanation, J. Catal. 432 (2024) 115439, https://doi.org/10.1016/j.jcat.2024.115439.
[44] D.C. Son, V. Thi, K. Anh, N.T. Thom, H. Le, T. Nguyen, L.V. Hai, Preparation and modification of zeolite A from kaolin for catalytic methanation of carbon dioxide, Vietnam J. Chem. 61 (2023) 170–177, https://doi.org/10.1002/vjch.202200027.
[45] K. Aimdate, A. Srifa, W. Koo-amornpattana, C. Sakdaronnarong, W. Klysubun, S. Kiatphuengporn, S. Assabumrungrat, S. Wongsakulphasatch, W. Kaveevivitchai, M. Sudoh, R. Watanabe, C. Fukuhara, S. Ratchahat, Natural kaolin-based Ni catalysts for CO2 methanation: on the effect of Ce enhancement and microwave-assisted hydrothermal synthesis, ACS Omega 6 (2021) 13779–13794, https://doi.org/10.1021/acsomega.1c01231.
[46] A.A. Alkhoori, A.A. Dabbawala, M.A. Baker, S. Mao, N. Charisiou, S.S. Hinder, M. Harfouche, D.H. Anjum, A. Goula, K. Polychronopoulou, From earth material to energy production:Ni-based modified halloysite catalysts for CO2 methanation, Appl. Clay Sci. 259 (2024) 107514, https://doi.org/10.1016/j.clay.2024.107514.
[47] F. Mateus, P. Teixeira, J.M. Lopes, C. Henriques, C. Bacariza, CO2 methanation on Ni catalysts supported over activated carbons derived from cork waste, Energy Fuel. 37 (2023) 8552–8562, https://doi.org/10.1021/acs.energyfuels.3c00908.
[48] S. Bahraminia, M. Anbia, Carbon dioxide methanation using Ni catalysts supported on low-cost Lynde Type A zeolite synthesized from pretreated Iranian coal gangue, Int. J. Hydrogen Energy 83 (2024) 842–855, https://doi.org/10.1016/j.ijhydene.2024.08.022.